

Article

Influence of Carbon Content on Tensile Properties of Pure High Manganese Austenitic Steel

Chen Chen ^{1,2,3,*}, Hua Ma ^{1,*}, Fei Wang ¹, Zhinan Yang ², Fucheng Zhang ^{1,2} and Zehui Yan ⁴

¹ State Key Laboratory of Metastable Materials Science and Technology, Yanshan University, Qinhuangdao 066004, China

² National Engineering Research Center for Equipment and Technology of Cold Strip Rolling, Yanshan University, Qinhuangdao 066004, China

³ Hebei Key Lab for Optimizing Metal Product Technology and Performance, Yanshan University, Qinhuangdao 066004, China

⁴ China Railway Baoji Bridge Group Co., Ltd., Baoji 721006, China

* Correspondence: chenchen@ysu.edu.cn (C.C.); mahua1617@163.com (H.M.)

Abstract: The tensile properties of high manganese austenitic steels with a carbon content ranging from 0.79 to 1.28 wt.% were tested. X-ray diffraction, electron backscattering diffraction, transmission electron microscopy, and optical microscopy were used to observe the microstructures after tensile deformation. Results showed that the strength and plasticity of these high manganese austenitic steels increased with increasing carbon content. The tensile strength and elongation of the 130Mn11 steel reached 941 MPa and 38.2%, respectively. The 0.79% carbon-containing steel (80Mn11) formed the most deformation twins at the same strain because of the low stacking fault energy, which resulted in a high strain hardening rate. However, this high strain hardening rate was unsustainable, and the tensile properties of the 80Mn11 steel were the worst, with its tensile strength nearly 200 MPa lower than that of the 130Mn11 steel. In the case of the 1.28% carbon-containing steel (130Mn11), the relatively low density of deformation twins, the large number of dislocations, and intensified DSA effect made the steel display a moderate strain hardening rate, which facilitated the sustainability of deformation, and an excellent combination of strength and plasticity were obtained.

Keywords: high manganese austenitic steels; deformation twins; dislocations; strain hardening rate; tensile properties



Citation: Chen, C.; Ma, H.; Wang, F.; Yang, Z.; Zhang, F.; Yan, Z. Influence of Carbon Content on Tensile Properties of Pure High Manganese Austenitic Steel. *Coatings* **2022**, *12*, 1622. <https://doi.org/10.3390/coatings12111622>

Academic Editor: Paolo Castaldo

Received: 22 September 2022

Accepted: 21 October 2022

Published: 26 October 2022

Publisher's Note: MDPI stays neutral with regard to jurisdictional claims in published maps and institutional affiliations.



Copyright: © 2022 by the authors. Licensee MDPI, Basel, Switzerland. This article is an open access article distributed under the terms and conditions of the Creative Commons Attribution (CC BY) license (<https://creativecommons.org/licenses/by/4.0/>).

1. Introduction

High manganese austenitic steel is widely used in railway, mining, automotive, and other industrial fields due to its excellent mechanical properties. For example, the railway frogs used all over the world are mainly made from Hadfield steel [1,2]. With the development of railway systems, the performance requirements of railway frog steels are getting higher. Therefore, it is urgent to optimize the comprehensive performance of high manganese austenitic steels. Factors that affect the mechanical properties of this kind of steel include chemical compositions, grain size, carbides, inclusions, and others [3,4]. The most basic and effective method to optimize its performance is to regulate the chemical composition [5]. The effect of carbon and manganese elements on the mechanical performance of the high manganese austenitic steel is obvious [6]. The solid dissolution of elements and the obstructing effect of Cottrell atmospheres on dislocation movement are important factors that affect the work-hardening characteristics [7]. The carbon and manganese content can also affect the formation of deformation twins by influencing the stacking fault energy, which could influence the mechanical properties of high manganese austenitic steel [8].

To date, there is not any unified theoretical explanation for the specific work hardening performance of high manganese austenitic steel. There are two main viewpoints on the

mechanism: dynamic strain aging (DSA) [9–11] and deformation twinning strengthening [12,13]. DSA strengthening was proposed by Dastur et al. [9], who concluded that the interaction of solute atoms with dislocations was the main reason for the specific work hardening performance of high manganese steel. However, Yeleussizova [12] believed that the obstructing effect of deformation twins to dislocations was the main cause of work hardening. Adler [13] claimed that with the formation of twins, the crystal structure of high manganese austenitic steel was converted from octahedral to tetrahedral interstices. With the increase in the tetrahedral interstices, a large number of carbon atoms occupied the space of the tetrahedron and severe lattice distortion was produced. Thus, it plays an important role in work hardening. As can be seen, solute atoms are important factors that affect the hardening capacity of high manganese austenitic steel in either theory. In our previous work [14–16], we also found that the strength and plasticity of high manganese austenitic steel can be improved greatly by adding a certain amount of Cr and N. Cr and N introduced solid-solution strengthening, and they can make it easier for deformation twins to form because of the reduced stacking fault energy. As a basic element in high manganese steel, carbon plays a key role in determining the microstructure and properties. However, how the varied carbon content affects the mechanical properties of high manganese austenitic steel is rarely reported.

In the present paper, high manganese austenitic steels with four different carbon contents were prepared and the influence of carbon content on the tensile properties was investigated.

2. Materials and Methods

The chemical composition of high manganese austenitic steels used in this study is listed in Table 1. The phosphorus and sulfur contents in the steels are lower than 0.001% and 0.003%, respectively, meaning the steels are examples of ultra-pure high manganese austenitic steel. The test steels were smelted in a vacuum induction furnace, and the cylindrical ingots were 50 kg in weight, with a diameter of 200 mm. The ingots were forged into square blocks with a size of 60 mm × 60 mm. The initial and finishing forging temperatures were 1150 and 950 °C, respectively. The steels were heated to 1050 °C. After holding for 1.5 h, water quenching was conducted to obtain a uniform austenite phase.

Table 1. Chemical compositions of high manganese austenitic steels (wt.%).

Test Steels	C	Mn	Si	p	S
80Mn11	0.79	11.0	0.39	<0.001	0.002
100Mn11	1.00	11.4	0.41	<0.001	0.003
120Mn11	1.15	11.1	0.41	<0.001	0.002
130Mn11	1.28	11.2	0.46	<0.001	0.002

Tensile tests were conducted on an MTS E45.105 static tensile machine at room temperature with a strain rate of $2 \times 10^{-3} \text{ s}^{-1}$. Cylindrical specimens with a whole length of 100 mm were chosen, and their gauge length and the diameter of the working part were 10 mm and 5 mm, respectively. The elongations were measured by an extensometer. The specimens were divided into two groups. The first group was stretched to fracture to obtain the strength and plasticity data. The second group was stretched to strains of 0.03, 0.10, and 0.20, without fracture.

The tensile deformation microstructures were observed under an Axiovert 200MAT optical microscope and an SU5000 scanning electron microscope (SEM, Hitachi High-Tech, Tokyo, Japan) equipped with an electron backscatter diffraction (EBSD) device. The observation surfaces were parallel to the tensile direction. Samples used for optical microscopy were mechanically polished and etched with a 4% nitric acid alcohol solution. An ion polishing machine was used to release the residual stress on the surface of the samples prepared for EBSD observation. Fine microstructures were further observed by a JEM-2010 transmission electron microscope (TEM). The thin foils used for TEM were prepared using

a precision ion polishing system (Gatan) after mechanically polishing to 30 μm using SiC paper. The dislocation density of the deformed samples was measured by X-ray diffraction (XRD) using a Cu target and K_{α} radiation. The characteristic wavelength λ was 1.540598 \AA . The scanning range was 20° – 120° and the step length was $2^{\circ}/\text{min}$. The dislocation density was then calculated based on the Williamson-Hall formula [17]:

$$\rho = 6\pi \frac{\varepsilon^2}{b^2} \quad (1)$$

where ρ is the dislocation density, ε is the microstrain, and b is the Burgers vector.

3. Results

3.1. Mechanical Properties

Figure 1 shows the tensile properties of the four test steels. With the increase in the carbon content in the selected range of the present study, the strength and plasticity are simultaneously improved (Figure 1a,b). The 130Mn11 steel obtained the best tensile properties out of the four test steels, with an ultimate tensile strength of 941 MPa and an elongation of 38.2%. The work-hardening exponent n , which reflects the ability of uniform plastic deformation of metals, hardly changed with the carbon content (Figure 1c). It is noteworthy that the occurrence of the serrations on the engineering stress-engineering stress curves increased with increasing carbon content in the test steels. The amplitude of the serration fluctuations also increases (Figure 1a). This indicates that the dynamic strain aging (DSA) effect intensifies with increasing carbon content [18].

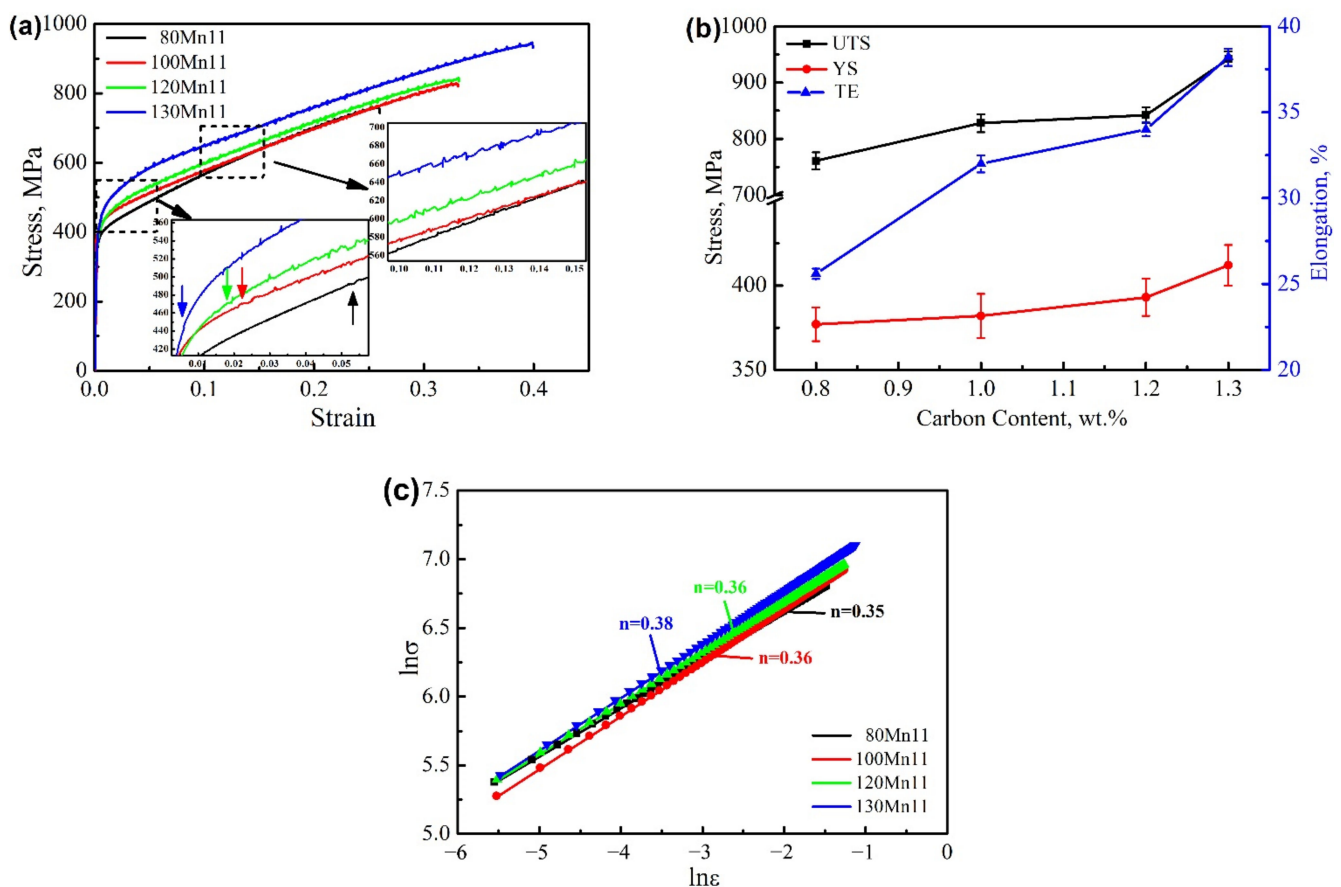


Figure 1. Tensile properties of test steels. (a) engineering stress-engineering strain curves; (b) strength and plasticity as a function of carbon content; and (c) work hardening exponent curves.

Figure 2 shows the strain hardening rate curves of the test steels with different carbon content. All four curves can be divided into three stages regardless of the carbon content. In the initial stage of deformation, the strain hardening rate drops sharply. After a certain amount of deformation, the strain hardening rate increases, and then the curves reach a plateau. In the last stage of the tensile deformation, the strain hardening rate decreases again until fracture [19]. These strain-hardening behaviors are determined by the microstructure evolution during the tensile deformation, e.g., deformation twins and dislocations. It is found that with increasing carbon content, the strain hardening rate shows a decreasing trend at the second stage, while the strain where the second stage starts increases. Moreover, the steel with the highest carbon content (130Mn11 steel) presents a low and slowly increasing strain hardening rate at stage II.

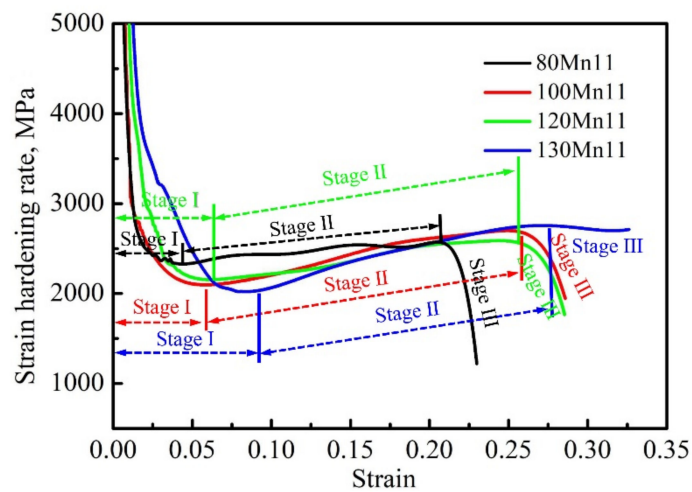


Figure 2. Strain hardening curves of test steels.

3.2. Deformation Microstructure

Figure 3 shows optical images of the test steels with a tension deformation strain of 0.2. It can be seen that the austenitic grains of the test steels are stretched along the tensile direction. Deformation bands are observed to be induced after tensile deformation in the austenitic grains, and the number of deformation bands in the test steels decreases with the increase in carbon content.

Figure 4 shows the TEM images of the 80Mn11 and 130Mn11 steels at a deformation strain of 0.2. As can be seen, a large number of deformation twins and dislocations are induced in the matrix of both steels. Parallel and intersected deformation twins are observed in the 80Mn11 steel, and dislocations have piled up at the twin boundaries (Figure 4a,b). The average deformation twin thickness of the 80Mn11 steel is measured to be 50 nm. Figure 4c,d show the TEM images of the 130Mn11 steel. Only parallel deformation twins are observed, and their average thickness is as large as 200 nm. Meanwhile, the number of deformation twins of the 130Mn11 steel is obviously smaller than that of the 80Mn11 steel, but there are more dislocations in the matrix.

Figure 5 shows the XRD patterns of the test steels at a tensile strain of 0.2. As can be seen, no characteristic peaks of martensite are observed under the selected deformation condition. Dislocation density was calculated based on the XRD patterns, and the results are listed in Table 2. With increasing carbon content in the test steels, the dislocation density increases gradually. The dislocation density of the 130Mn11 steel was calculated to be nearly twice that of the 80Mn11 steel. These results agree well with that shown in Figure 4. With the results obtained in Figure 4 and Table 2, the changing trend of deformation twin and dislocation number was found to differ between the steels, which could be the key factor influencing their mechanical properties.

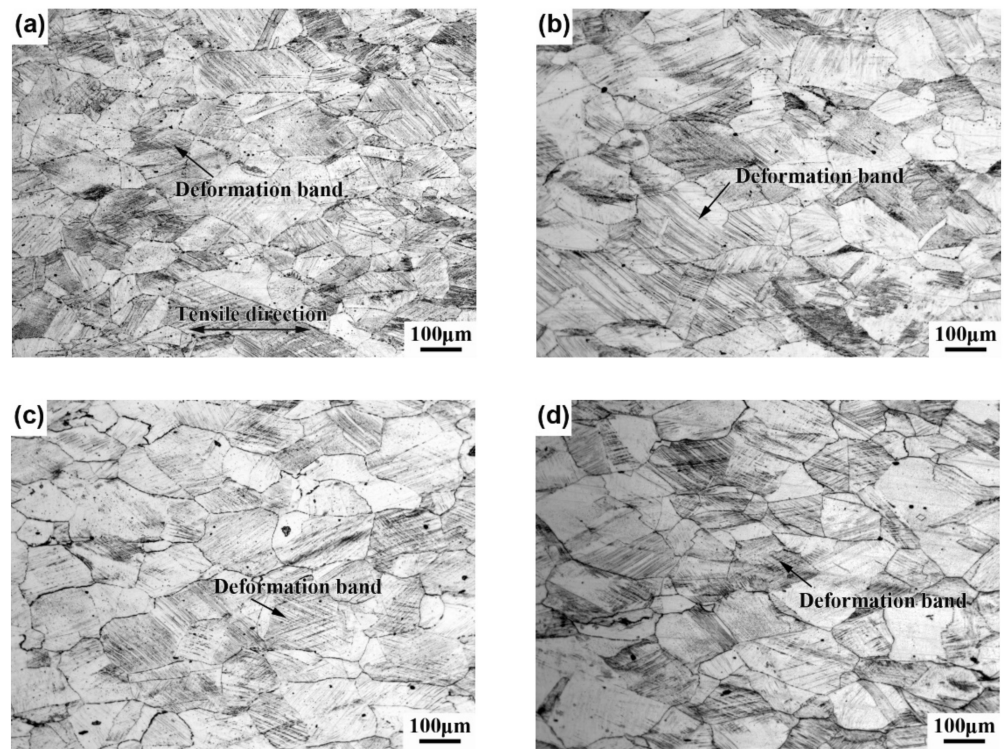


Figure 3. Optical images of test steels with a tension deformation strain of 0.2. (a) 80Mn11; (b) 100Mn11; (c) 120Mn11; and (d) 130Mn11.

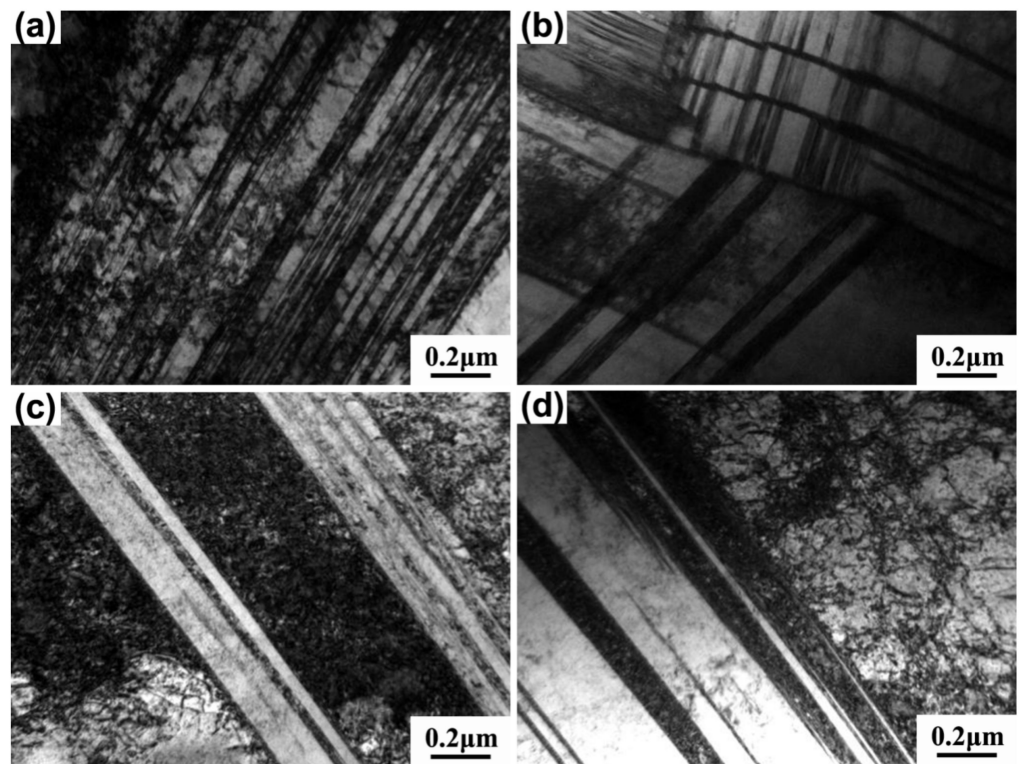


Figure 4. TEM images of 80Mn11 (a,b) and 130Mn11 (c,d) steels at a tensile strain of 0.2.

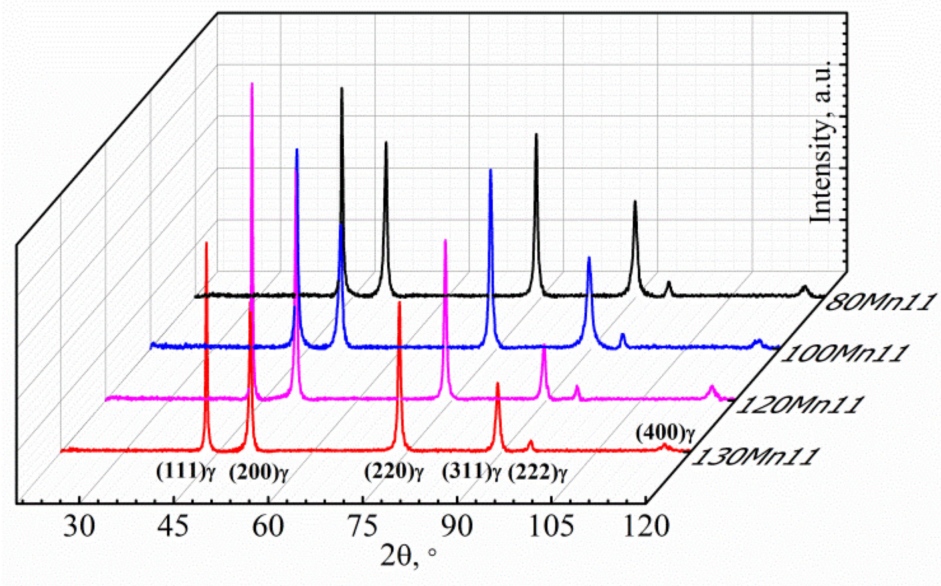


Figure 5. XRD patterns of test steels with different carbon content at a tensile strain of 0.2.

Table 2. Dislocation densities of test steels with different carbon content at a tensile strain of 0.2 ($\times 10^{15} \cdot \text{m}^{-2}$).

Test Steels	80Mn11	100Mn11	120Mn11	130Mn11
Dislocation density	2.52	3.08	3.93	4.79

4. Discussion

The chemical composition of high manganese steels influences microstructure evolution, which in turn determines the work-hardening behavior and mechanical properties [20]. For the test steels selected in the present study, the stacking fault energy (SFE) will be increased from $\sim 19 \text{ mJ/m}^2$ to $\sim 32 \text{ mJ/m}^2$ with the increase in carbon content, which is calculated based on a thermodynamic model [21]—i.e., the 80Mn11 steel possesses the lowest SFE of the four test steels. A low SFE favors the formation of deformation twins [14]. For this reason, deformation twins are induced in the 80Mn11 steel even at a small strain of 0.03, as shown in Figure 6a; while in the 130Mn11 steel, only a few annealing twins are observed (Figure 6b). The difference in deformation twin evolution in the test steels is also confirmed when the deformation strain reached 0.1 and 0.2 (Figures 4 and 6c,d). At the same time, the high content of carbon in the test steels results in a high number of solute atoms in the matrix. The blocking effect of solute atoms, especially the carbon atoms, on the dislocation motion promotes the accumulation of dislocations [22], and high-density dislocations are induced in the test steels with high carbon content (Table 2). As a result, the interaction between dislocations and solute atoms is further intensified, and an active DSA effect is observed in the test steels with high carbon content (Figure 1).

As an effective obstacle to dislocation movement, the early generation of deformation twins increases the strain hardening rate of the 80Mn11 steel, and the strain range of stage I in the strain hardening rate curve is the minimum in the four test steels (Figure 2). With the increase in carbon content, the strain range of stage I is enlarged, indicating a relatively slow microstructure evolution to improve the hardening behavior.

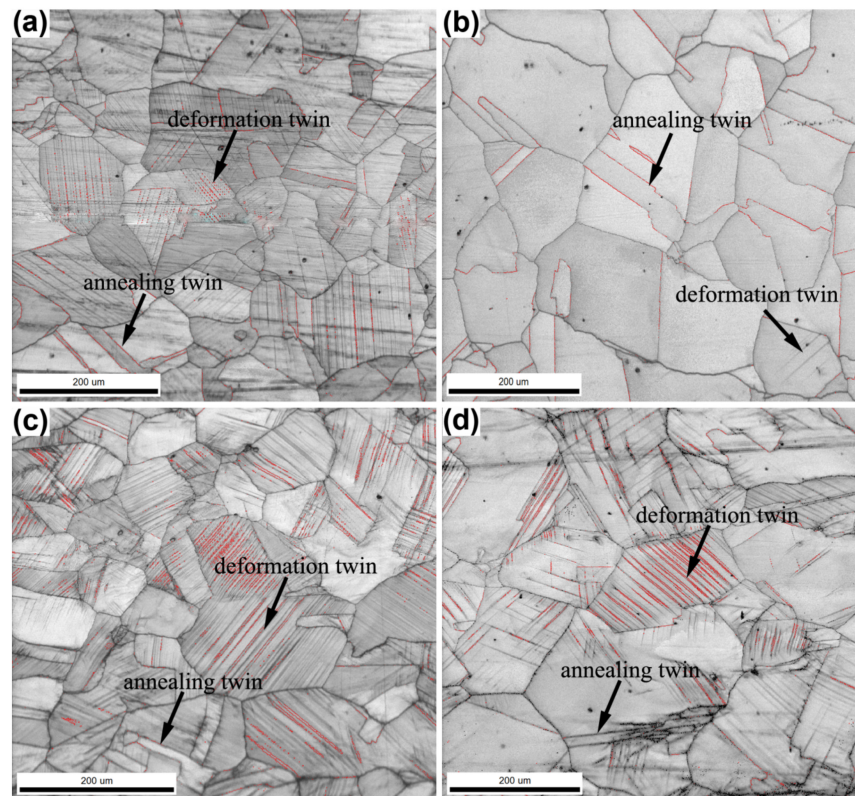


Figure 6. EBSD images of two test steels after tensile deformation with different deformation strains. (a) 80Mn11 steel—0.03; (b) 130Mn11 steel—0.03; (c) 80Mn11 steel—0.10; and (d) 130Mn11 steel—0.10.

As the deformation continues, the strain-hardening curves enter the second stage. Since the deformation twin density remains high in the 80Mn11 steel, its strain hardening rate remains the highest at stage II in the four test steels. However, the strain hardening rate value of the 80Mn11 steel remains also constant, while that of the 130Mn11 steel increases gradually at stage II (Figure 2). For the test steels selected in the present study, deformation twins, dislocations, and the DSA effect are the main hardening factors [9]. High-density twins are induced in the 80Mn11 steel (Figures 4a,b and 6a,c), but the dislocation density is low (Table 2), and the DSA effect is inactive (Figure 1). In this situation, the strain hardening rate cannot be further improved. When the density of deformation twins reaches a saturation value, the strain hardening rate decreases sharply, and the curve enters the third stage (Figure 2). However, for the 130Mn11 steel with a relatively low density of deformation twins (Figures 4 and 6), the high density of dislocations and intensified DSA effect (Figure 1a and Table 2) make the strain hardening rate maintain a moderate but slowly increasing value (Figure 2). This kind of strain-hardening behavior is more favorable for improving the strength and plasticity of steels [20]. As a result, the 130Mn11 steel obtained the best tensile properties of the four test steels. In the case of the yield strength of the four test steels, it increased slightly with increasing carbon content because of the solution-strengthening effect when the grain sizes were largely consistent [23].

5. Conclusions

The tensile properties of four high manganese steels with varied carbon content were tested in the present study. The deformation microstructures were observed to explain the difference in mechanical properties. The following conclusions can be drawn:

1. The strength and plasticity of the test steels increased with increasing carbon content in the selected range. The 130Mn11 steel obtained the optimum tensile properties, with a tensile strength of 941 MPa and an elongation of 38.2%.

2. The low carbon content in the 80Mn11 steel promoted the formation of deformation twins because of the low SFE. The high density of deformation twins makes the 80Mn11 steel obtain the highest work hardening rate at the initial stage of tensile deformation. However, it's detrimental to the sustainability of deformation. As a result, the strength of the 80Mn11 steel was nearly 200 MPa lower than that of the 130Mn11 steel.
3. The high carbon content in the 130Mn11 steel intensified the DSA effect and facilitated the accumulation of dislocations. Combined with a relatively low density of deformation twins, the 130Mn11 steel presented a moderate strain hardening rate, which allowed the deformation to continue to a greater strain. This working hardening characteristic made the 130Mn11 steel obtain the optimum tensile properties.

Author Contributions: Methodology, C.C. and H.M.; software, Z.Y. (Zehui Yan); investigation, C.C., H.M. and F.W.; writing—original draft preparation, C.C.; writing—review and editing, C.C., Z.Y. (Zhinan Yang), F.Z. and Z.Y. (Zehui Yan); funding acquisition, F.Z. All authors have read and agreed to the published version of the manuscript.

Funding: The authors gratefully acknowledge the National Natural Science Foundation of China (52201143 and 52171049) and the Hebei Province Innovation Ability Promotion Project (22567609H).

Institutional Review Board Statement: Not applicable.

Informed Consent Statement: Not applicable.

Data Availability Statement: All data that support the findings of this study are included within the article.

Conflicts of Interest: The authors declare no conflict of interest.

References

1. Zhang, F.C. Research progress of high manganese steel crossing materials. *J. Yanshan Univ.* **2010**, *34*, 189–193.
2. Yang, Z.N.; Zhang, F.C.; Zhang, M. Study on mechanical impact pre-hardening technology of high manganese steel crossing. *J. Mech. Eng.* **2011**, *47*, 20–24. [[CrossRef](#)]
3. Chen, C.; Zhang, F.; Lv, B.; Ma, H.; Wang, L.; Zhang, H.; Shen, W. Asynchronous effect of N+Cr alloying on the monotonic and cyclic deformation behaviors of hadfield steel. *Mater. Sci. Eng. A* **2019**, *761*, 138015. [[CrossRef](#)]
4. Chen, C.; Lv, B.; Ma, H.; Sun, D.; Zhang, F. Wear behavior and the corresponding work hardening characteristics of Hadfield steel. *Tribol. Int.* **2018**, *121*, 389–399. [[CrossRef](#)]
5. Anijdan, S.H.M.; Sabzi, M. The effect of heat treatment process parameters on mechanical properties, precipitation, fatigue life, and fracture mode of an austenitic Mn Hadfield steel. *J. Mater. Eng. Perform.* **2018**, *27*, 5246–5253. [[CrossRef](#)]
6. Yin, H.X.; Zhao, A.M.; Zhao, Z.Z. Effect of Mn content on microstructure and mechanical properties of a low carbon medium-manganese TRIP steel. *J. Mater. Sci. Technol.* **2014**, *22*, 11–15.
7. Zu, F.Q.; Li, X.Y.; Liu, L.J. Research on microstructure and work hardening mechanism of high manganese steel by simulating actual working condition. *Trans. Mater. Heat Treat.* **2006**, *27*, 71–74.
8. Li, D.; Qian, L.; Wei, C.; Liu, S.; Zhang, F.; Meng, J. The tensile properties and microstructure evolution of cold-rolled Fe–Mn–C TWIP steels with different carbon contents. *Mater. Sci. Eng. A* **2022**, *839*, 142862. [[CrossRef](#)]
9. Dastur, Y.N.; Leslie, W.C. Mechanism of work hardening in hadfield manganese steel. *Metall. Trans. A* **1981**, *12*, 749–759. [[CrossRef](#)]
10. Owen, W.S.; Grujicic, M. Strain aging of austenitic Hadfield manganese steel. *Acta Mater.* **1998**, *47*, 111–126. [[CrossRef](#)]
11. Zuidema, B.K.; Subramanyam, D.K.; Leslie, W.C. The effect of aluminum on the work hardening and wear resistance of hadfield manganese steel. *Metall. Trans. A* **1987**, *18*, 1629–1639. [[CrossRef](#)]
12. Yeleussizova, A.A.; Skakov, M.K.; Zhilkashinova, A.M. Deformation Twinning in Hadfield Steel. *Adv. Mater. Res.* **2013**, *772*, 62–67. [[CrossRef](#)]
13. Alder, P.H.; Olson, G.B.; Owen, W.S. Strain hardening of hadfield manganese Steel. *Metall. Trans. A* **1986**, *17*, 1725–1737.
14. Chen, C.; Zhang, F.C.; Wang, F. Effect of N+Cr alloying on the microstructures and tensile properties of Hadfield steel. *Mater. Sci. Eng. A* **2016**, *679*, 95–103. [[CrossRef](#)]
15. Kang, J.; Zhang, F.C.; Long, X.Y. Synergistic enhancing effect of N+C alloying on cyclic deformation behaviors in austenitic steel. *Mater. Sci. Eng. A* **2014**, *610*, 427–435. [[CrossRef](#)]
16. Kang, J.; Zhang, F.C.; Long, X.Y. Cyclic deformation and fatigue behaviors of Hadfield manganese steel. *Mater. Sci. Eng. A* **2014**, *591*, 59–68. [[CrossRef](#)]

17. Pan, L.; He, W.; Gu, B.P. Effects of electric current pulse on dislocation density and residual stresses of 45 carbon steel workpieces. *Trans. Metal. Heat Treat.* **2015**, *36*, 134–138.
18. Kim, J.-K.; Chen, L.; Kim, H.-S.; Kim, S.-K.; Estrin, Y.; De Cooman, B.C. On the tensile behavior of high-manganese twinning-induced plasticity steel. *Metall. Mater. Trans. A* **2009**, *40*, 3147–3158. [[CrossRef](#)]
19. Xiong, R.; Liu, Y.; Si, H.; Peng, H.; Wang, S.; Sun, B.; Chen, H.; Kim, H.S.; Wen, Y. Effects of Si on the microstructure and work hardening behavior of Fe-17Mn-1.1 C-xSi high manganese steels. *Met. Mater. Int.* **2021**, *27*, 3891–3904. [[CrossRef](#)]
20. Zhao, T.; Wang, F.; Chen, C.; Ma, H.; Yang, Z.; Zhang, F.; Tang, T. Effect of Mn content and strain rate on mechanical properties of high-C high-Mn austenitic steel. *Mater. Sci. Eng. A* **2022**, *851*, 143653. [[CrossRef](#)]
21. Curtze, S.; Kuokkala, V.-T.; Oikari, A.; Talonen, J.; Hänninen, H. Thermodynamic modeling of the stacking fault energy of austenitic steels. *Acta Mater.* **2011**, *59*, 1068–1076. [[CrossRef](#)]
22. Bouaziz, O.; Allain, S.; Scott, C.P.; Cugy, P.; Barbier, D. High manganese austenitic twinning induced plasticity steels: A review of the microstructure properties relationships. *Curr. Opin. Solid State Mater. Sci.* **2011**, *15*, 141–168. [[CrossRef](#)]
23. Jacob, R.; Sankaranarayanan, S.R.; Babu, S.P.K. Recent advancements in manganese steels—A review. *Mater. Today Proc.* **2020**, *27*, 2852–2858. [[CrossRef](#)]